Evaluation of Effective Material Parameters of CNT-reinforced Composites via 3D BEM

F.C. Araújo[1] and L.J. Gray[2]

Abstract: In recent years, carbon nanotubes (CNTs) have been widely employed to build advanced composites. In this work, a Boundary Element Method (BEM) is applied to 3D representative volume elements (RVEs) to estimate mechanical properties of CNT-based composites. To model the thin-walled nanotubes, special integration procedures for calculating nearly-strongly-singular integrals have been developed. The generic BE substructuring algorithm allows modeling complex CNT-reinforced polymers, containing any number of nanotubes of any shape (straight or curved). The subregion-by-subregion strategy, based on Krylov solvers, makes the independent generation, assembly, and storage of the many parts of the complete BE model possible. Thus, significant memory and CPU-time reductions are achieved in avoiding working with an explicit global system of equations. Further CPU-time reduction is obtained by employing a matrix-copy option for repeated subregions. Several applications will illustrate the ability of this algorithm to analyze CNT-based composites.

Keyword: CNT-based composites, 3D BE formulations, singular and quasi-singular quadratures, subregion-by-subregion techniques, the boundary element method.

1 Introduction

Due to their exceptionally good physical properties, carbon nanotubes (CNTs) have been extensively exploited to develop a new generation of materials. Reported results show that they substantially improve the physical characteristics of polymeric matrices, e.g. stiffness, strength, thermal conductivity. Physically, CNTs consist of covalently bonded carbon atoms; geometrically, they are hollow, seamless, cylindrical tubes formed by a single or several graphene layers. In structural engineering, CNTs have been employed as reinforcing elements (fibers) to manufacture advanced light-weight composites. Qian, Dickey, Andrews, and Rantell (2000) report that with a weight increase of 1%, a gain between 36% and 42% in stiffness, and of approximately 25% in tensile strength can be achieved. In fact, attracted by the technological importance of nano-materials, a surge of research in nanomechanics has taken place, generally beginning in the early 90s, when CNTs were discovered [Iijima (1991)]. Srivastava1 and Atluri (2002) give a brief review of computational nanotechnology, highlighting its relevance in engineering and computational approaches. Ghoniem and Cho (2002) discuss the available formulations and their validity in the light of the different scales, going from atomistic to continuum models. Taking into account the dimensions of nanosystems, it is evident that molecular dynamics (MD) formulations, which directly deal with the interatomic interaction, should be considered. Nevertheless, employing atomic-level-based methods is, even for the present-day computers, limited to very small models, over very short times. In Namilae, Chandra, Srinivasan, and Chandra (2007), information is given about the computational effort for running molecular-dynamics-based models. In general, this fact (computational effort) has led to attempts to use continuum-mechanics (CM) models.

In Yakobson, Brabec, and Bernholc (1996), MD simulations and simple continuum shell models were employed to predict buckling properties in

---

[1] Dept Civil Eng, UFOP, Ouro Preto, MG, Brazil; visitor at the Oak Ridge National Laboratory, TN, U.S.A.
[2] Oak Ridge National Laboratory, TN, U.S.A

single-walled CNTs. The results revealed that continuum shell formulations can be satisfactorily applied to CNTs. More recently, continuum cylindrical shell models [He, Kitipornchai, and Liew (2005); Kitipornchai, He, and Liew (2005)], and a shell FE-based approach [Pantano, Parks, and Boyce (2004)] have been applied to single and multi-walled CNTs. Again, results in very good agreement with MD simulations were obtained. Wang, Ma, Zhang, and Ang (2006) also showed that solid shell finite elements are applicable to model CNTs. In case of multi-walled CNTs, they adopted spring-like models to simulate the van der Waals forces between the nanotubes. CM-based formulations applied to nanosolids are also reported by Chen, Dorgan Jr, McIlroy, and Aston (2006). Based upon experiments in silver nanowires, they concluded that classical beam and 3D FE analyses can accurately describe their bending behavior, as long as the boundary conditions are realistically enforced. Finally, Lau, Chiparab, Linga, and Hui (2004) review the validity of different approaches to estimating the mechanical properties of carbon nanotubes for advanced composite structures.

In Chen and Liu (2004), a CM-based strategy has been applied to study CNT-reinforced composites. They employed a 3D quadratic solid (brick) finite element to model representative volume elements containing a single CNT (single-unit-cell RVEs), and a 2D quadratic 8-node finite element to model multi-unit-cell RVEs (containing many CNTs). In the present work, single-unit and multi-unit cells are also considered to characterize CNT-reinforced composites, however 3D boundary element techniques are employed. In general, the strategy has two main parts: a robust subregion-by-subregion (SBS) technique, necessary for coping with heterogeneous materials, and efficient integration procedures, needed for evaluating the singular and nearly-singular integrals that arise. The SBS technique [Araújo, Silva, and Telles (2006)] is based on the use of Krylov solvers, allowing the treatment of composites consisting of a large number of components (e.g. matrix-material substructures and fibers). Here, the diagonal-preconditioned biconjugate gradient

solver (J-BiCG) is employed. Moreover, to efficiently model composites containing geometrically and physically identical substructures, a matrix-copy option is considered in this study. The matrices for repeated subregions are immediately obtained simply by copy and rotation transformations. Finally, the SBS technique utilizes discontinuous boundary elements [Araújo, Silva, and Telles (2006, 2007)], which enormously simplify the modeling of complex coupled subregions.

An additional challenge in applying boundary-element methods (BEM) to composites is the accurate and efficient evaluation of singular and nearly-singular integrals. These integrals result not only from modeling thin-walled components but also from employing discontinuous elements. For weakly-singular and nearly-weakly-singular integrals, numerical quadratures that combine triangle and polynomial coordinate transformations have proven to be efficient [Chen and Liu (2005); Araújo, Silva, and Telles (2006)]. In case of the nearly-strongly-singular integrals, the line-integral approach proposed by Liu (1998) is employed. This method is based on employing the Stokes' theorem to convert surface integrals to 1D integrals. In Chen and Liu (2005), quadratures that combine triangle and polynomial transformations were also applied to improve the accuracy of the surface integrals involved in the line-integral approach. In Araújo and Gray (2008), the line-integral approach was improved by applying a cubic polynomial transformation [Telles (1987)] to the nearly-strongly-singular line integrals. In this work, additional speed and accuracy are provided by using analytical integration where possible. This considerably increases the effectiveness of the SBS technique for composites and other engineering systems.

3D simulations of CNT-composites based on square-packed and hexagonal-packed fiber arrays are considered for verifying the robustness of the strategy. Possible future developments are also commented upon.

2 3D BE modeling of CNT-reinforced composites

Assuming that continuum mechanics models can satisfactorily describe the deformation of carbon nanotubes (CNT) under stress, analysis methods for regular solids can be applied to yield insights into the micromechanics of CNT-reinforced composites. Thereby, the prediction of their effective constants, the construction of appropriate failure theories, and their design for achieving particular performance can be accomplished. Here, a 3D boundary element technique is employed to model general CNT-based composites. The key new techniques required are special integration procedures for coping with nearly-singular integrals, and a robust generic substructuring strategy. The special integration procedures can accurately and efficiently handle the thin-walled domains present in the composite, while the substructuring technique is essential for dealing with the complex heterogeneity. Moreover, the substructuring technique can be easily exploited for developing parallel codes, essential for solving large-scale composite models.

2.1 Special integration quadratures

In applying boundary integral methods to solids containing thin-walled domains, e.g. composites consisting of discrete reinforcing elements or particles in a polymer matrix, the efficient computation of singular and nearly-singular integrals demand special attention. Standard numerical integration procedures lead to either high matrix-assembly CPU time and/or inaccurate solutions. In 3D elasticity boundary-element formulations, the surface integrals are of the form

$$\int_{\Gamma_e} p_{ik}^*(\chi;\xi)u_i(\chi)d\Gamma(\chi), \tag{1a}$$

$$\int_{\Gamma_e} u_{ik}^*(\chi;\xi)p_i(\chi)d\Gamma(\chi), \tag{1b}$$

where u_{ik}^* and p_{ik}^* are the Kelvin fundamental kernels, u_i and p_i are the boundary displacement and traction respectively, and Γ_e is the surface of the e-th boundary element. In this study, a quadrature based on combining triangle-polar

and polynomial coordinate transformations is employed to compute weakly-singular and nearly-weakly-singular surface integrals. The nearly-strongly-singular integrals are evaluated by the line-integral approach proposed in Liu (1998) and Chen and Liu (2005). These procedures are described below. Note too that the strongly-singular integrals (Cauchy principal value integrals), are calculated indirectly by means of rigid-body displacements; their accuracy will therefore depend upon the accurate evaluation of the weakly-singular and nearly-weakly-singular integrals.

2.1.1 Weakly-singular and quasi-singular integrals

Previous studies [Chen and Liu (2005); Araújo, Silva, and Telles (2006, 2007)] have shown that quadratures derived by combining triangle-polar and polynomial coordinate transformations are more efficient than the corresponding pure coordinate-transformation-based quadratures for evaluating weakly-singular and nearly-weakly-singular surface integrals. These strategies are therefore employed in this study.

Assuming that f_{ik}^* is a generic singular kernel, a combined coordinate-transformation-based quadrature procedure can be expressed as [Araújo, Silva, and Telles (2006, 2007)]

$$\int_{\Gamma_e} f_{ik}^*(\chi;\xi)h_q d\Gamma(\chi)$$
$$= \int_{-1}^{1}\int_{-1}^{1} f_{ik}^*[(\eta_1,\eta_2);\xi]h_q(\eta_1,\eta_2)J^{(e)}(\eta_1,\eta_2)$$
$$d\eta_1 d\eta_2$$
$$= \frac{1}{4}\sum_{g=1}^{n_t}\int_{-1}^{1}\int_{-1}^{1} f_{ik}^*[(\zeta_1(\gamma),\zeta_2);\xi]\, h_q[\zeta_1(\gamma),\zeta_2]$$
$$\times J^{(e)}[\zeta_1(\gamma),\zeta_2]\,[1+\zeta_1(\gamma)]A_g J_p(\gamma)d\gamma d\zeta_2, \tag{2}$$

where $J^{(e)}$ is the element Jacobian, h_q is the element interpolation function, n_t the number of triangular subdomains, A_g the area of the g-th triangular subdomain, and $\zeta_1(\gamma)$ defines the polynomial transformation adopted for the ζ_1 direction. For the cubic coordinate transformation employed in the application calculations in section 4,

the mapping and its Jacobian are given by

$$\zeta_1 = \zeta_1(\gamma) = \frac{(\gamma - \overline{\gamma})^3 + \overline{\gamma}(\overline{\gamma}^2 + 3)}{(1 + 3\overline{\gamma}^2)}, \tag{3a}$$

$$J_p(\gamma) = \frac{3(\gamma - \overline{\gamma})^3}{(1 + 3\overline{\gamma}^2)}, \tag{3b}$$

with

$$\overline{\gamma} = \left(\overline{\zeta}_1 \zeta^* + |\zeta^*|\right)^{\frac{1}{3}} + \left(\overline{\zeta}_1 \zeta^* - |\zeta^*|\right)^{\frac{1}{3}} + \overline{\zeta}_1, \tag{3c}$$

$$\zeta^* = \overline{\zeta}_1^2 - 1, \tag{3d}$$

$\overline{\zeta}_1$ being the ζ_1 natural abscissa of the singular point [Telles (1987)]. Note that no polynomial transformation is needed in the ζ_2 direction, and after applying the triangle polar coordinate transformation in the ζ_1 direction, $\overline{\zeta}_1 = -1$. [Araújo, Silva, and Telles (2006, 2007)]. In the combined coordinate-transformation-based quadrature, higher-order polynomials may be easily considered [Chen and Liu (2005); Araújo, Silva, and Telles (2006)]. The corresponding numerical quadrature will be denoted by $I^{(2)}(n_1, n_2)$, where n_1 and n_2 are the numbers of integration points in ζ_1 and ζ_2 directions respectively.

2.1.2 Strongly-quasi-singular integrals

Nearly-strongly-singular integrals arise in discontinuous BE formulations and in the modeling of thin-walled domains. These integrals pose special difficulties and may lead to inaccurate response if not handled correctly. Here, the line-integral approach presented by Liu (1998) for elastostatics is employed to evaluate this type of integral. The integral (1a) is first regularized in the form

$$\int_{\Gamma_e} p_{ik}^*(\chi; \xi) u_i(\chi) d\Gamma(\chi)$$

$$= \int_{\Gamma_e} p_{ik}^*(\chi; \xi) [u_i(\chi) - u_i(\xi')] d\Gamma(\chi)$$

$$+ u_i(\xi') \int_{\Gamma_e} p_{ik}^*(\chi; \xi) d\Gamma(\chi), \tag{4}$$

where ξ' is the projection of ξ onto Γ_e [Liu (1998); Chen and Liu (2005)]. As the first integral on the right-hand side of (5) is at most nearly-weakly-singular, the combined-transformation-based quadrature for surface integrals discussed

above can be applied. To indicate that this quadrature is applied to the surface integral inside the line-integral approach, it will be denoted by $L^{(2)}(n_1, n_2)$. The last integral in (5) can be converted into a line integral by applying Stokes' theorem [see Liu (1998)], resulting in

$$\int_{\Gamma_e} p_{ik}^*(\chi; \xi) d\Gamma(\chi)$$

$$= \frac{\delta_{ik}}{4\pi} \oint_{C_e} \left[\frac{r_3'(\chi)}{r(\chi)} - 1 \right] \frac{(\hat{\rho}_m \hat{v}_m)(\hat{t}_n \hat{\eta}_n)}{\rho} dC(\chi)$$

$$- \frac{1}{4\pi} e_{ikl} \oint_{C_e} \left(\frac{1}{r} \right) ds_l(\chi)$$

$$+ \frac{1}{8\pi(1-\upsilon)} e_{iml} \oint_{C_e} r_{,km} ds_l(\chi). \tag{5}$$

Here C_e is the contour of the element, $\mathbf{s}(\chi)$ its tangent vector, υ is the Poisson's ratio, e_{ikl} is the permutation tensor, $r = \|\mathbf{r}\| = \|\chi - \xi\|$, $\boldsymbol{\rho}$ is the projection of $\mathbf{r}$ onto the $x_1' x_2'$-plane, $\hat{\boldsymbol{\rho}}$ the unit vector along $\boldsymbol{\rho}$, $\hat{\mathbf{t}}$ the tangent unit vector along C_e, $\hat{\boldsymbol{\eta}}$ the unit vector along the projection vector of $\hat{\mathbf{t}}$ onto the $x_1' x_2'$-plane, and $\hat{\boldsymbol{v}}$ the unit vector along $\hat{\boldsymbol{\eta}} \times \mathbf{e}_3'$, $\mathbf{e}_3'$ being the unit vector along x_3'. To evaluate the first integral on the right-hand side of (6), a local $x_1' x_2' x_3'$ reference system, with origin at ξ and x_3'-axis along the vector $\xi' - \xi$, is considered. Details of the integration variables are shown in Fig. 1. The last two integrals in (6) refer to the global $x_1 x_2 x_3$ system.

The first integral in (6) is a measure of the solid angle $\Phi^{(\xi,e)}$ subtended by the boundary element Γ_e at ξ. This integral is well-behaved and can be conveniently computed by regular Gauss quadrature. The other line integrals are nearly-strongly-singular and again require special integration procedures. In Araújo and Gray (2008), a cubic polynomial transformation has been applied to improve the efficiency of integration algorithm for these integrals. Mapped in the interval $-1 \leq \gamma \leq 1$, Eq. (6) becomes

$$f_{ki} = \left(\frac{\Phi^{(\xi,e)}}{4\pi} \right) \delta_{ik} - \frac{1}{4\pi} e_{ikl} A_l$$

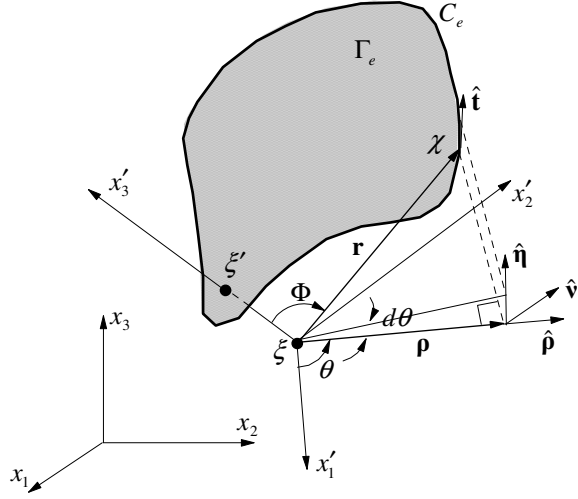$$+ \frac{1}{8\pi(1-\upsilon)} e_{iml} B_{lkm}, \tag{6}$$

Figure 1: Integration variables for computing $\Phi^{(\xi,e)}$

with

$$\Phi^{(\xi,e)} = \sum_{j=1}^{n_s} \int_{-1}^{1} f_1[\zeta(\gamma)] J_{C_e}^{(j)}[\zeta(\gamma)] J_P(\gamma) d\gamma, \quad (7)$$

$$A_l = \sum_{j=1}^{n_s} \int_{-1}^{1} \left(\frac{1}{r}\right) \frac{\partial x_l^{(j)}}{\partial \zeta} J_P(\gamma) d\gamma, \quad (8)$$

$$B_{lkm} = \sum_{j=1}^{n_s} \int_{-1}^{1} (r_{,km}) \frac{\partial x_l^{(j)}}{\partial \zeta} J_P(\gamma) d\gamma, \quad (9)$$

where in expressions (8)-(10) n_s is the number of edges of the boundary element (3 or 4, each edge with a single integration element), J_P is the Jacobian of the polynomial transformation, $J_{C_e}^{(j)}$ is the Jacobian of the j-th edge element (2- or 3-node 1D elements), and

$$f_1(\zeta) = [\frac{r_3'(\zeta)}{r(\zeta)} - 1] \cdot \frac{[\hat{\rho}_m(\zeta)\hat{v}_m(\zeta)][\hat{t}_n(\zeta)\hat{\eta}_n(\zeta)]}{\rho(\zeta)}. \quad (10)$$

Note that for cubic polynomial transformation, ζ_1 and J_p are given by Eqs. (4a) and (4b) respectively. If no coordinate transformation is applied, $\zeta_1(\gamma) = \gamma$ and $J_p(\gamma) = 1$. In the integration algorithm, the coordinate transformation is applied only for the nearly singular edges. Integration over the well-behaved edges is carried

out by standard Gauss quadrature. The 1D numerical quadrature obtained by employing relation (7) will be denoted by $^{num}L^{(1)}(m)$, where m is the number of integration points adopted, and the superscript num indicates that closed expressions are not employed for any line integral; the evaluation is exclusively numerical.
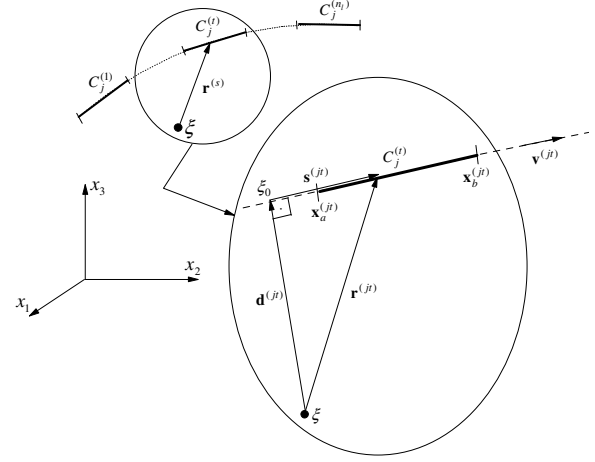

Figure 2: Integration variables for the line integrals

Observing that the strongly-singular kernels in Eq. (6) (involved in the two last integrals) are simple expressions, analytical integration over linear geometrical segments can be easily carried out. To accomplish this, the integration variables depicted in Fig. 2 are considered. Moreover, by subdividing the boundary-element contours (edges) in n_l subelements, the strategy can be applied to higher-order boundary elements. The integrals in Eq. 9 and (10) become

$$A_l = \oint_{C_e} \left(\frac{1}{r}\right) ds_l(\chi) = \sum_{j=1}^{n_s} \sum_{t=1}^{n_l} v_l^{(jt)} I_1^{(jt)}, \quad (11)$$

$$B_{lkm} = \oint_{C_e} r_{,km} ds_l(\chi)$$
$$= \delta_{km} A_l$$
$$- \sum_{j=1}^{n_s} \sum_{t=1}^{n_l} v_l^{(jt)} \left[a_{mk} I_2^{(jt)} + b_{mk} I_3^{(jt)} + c_{mk} I_3^{(jt)} \right], \quad (12)$$

with

$$I_1^{(jt)} = \int_{s_1}^{s_2} \frac{ds}{(d^2+s^2)^{1/2}}, \tag{13}$$

$$I_2^{(jt)} = \int_{s_1}^{s_2} \frac{ds}{(d^2+s^2)^{1/2}}, \tag{14}$$

$$I_3^{(jt)} = \int_{s_1}^{s_2} \frac{s\,ds}{(d^2+s^2)^{3/2}}, \tag{15}$$

$$I_4^{(jt)} = \int_{s_1}^{s_2} \frac{s^2\,ds}{(d^2+s^2)^{3/2}}. \tag{16}$$

Here $d = \left\|\mathbf{d}^{(jt)}\right\|$, $s = \left\|\mathbf{s}^{(jt)}\right\|$, and the integration limits s_1 and s_2 are determined as a function of the position of ξ_0, the projection of ξ onto the line containing the t-th subelement on the j-th edge of the boundary element. Furthermore, by defining the scalar α by means of the relationship

$$\zeta_0 - \mathbf{x}_a^{(jt)} = \alpha \mathbf{v}^{(jt)}, \tag{17}$$

where $\mathbf{v}^{(jt)}$ is the unit vector in the direction of the integration subelement and $\mathbf{x}_a^{(jt)}$ its initial node (see Fig. 2), the closed-form expressions for the definite integrals (13)-(16) are given according to the three cases below.

Case I : $\alpha \leq 0$.

Here, $s_1 = \min(l_1, l_2)$, $s_2 = \max(l_1, l_2)$, with

$$\begin{aligned} l_1 &= \left\|\mathbf{x}_a^{(jt)} - \xi_0\right\|, \\ l_2 &= \left\|\mathbf{x}_b^{(jt)} - \xi_0\right\|. \end{aligned} \tag{18}$$

One has:

$$I_1^{(jt)} = \left| \ln[(d^2+s_2^2)^{\frac{1}{2}} + s_2] - \ln[(d^2+s_1^2)^{\frac{1}{2}} + s_1] \right|, \tag{19}$$

$$I_2^{(jt)} = \frac{1}{d^2} \left| \frac{s_2}{(d^2+s_2^2)^{1/2}} - \frac{s_1}{(d^2+s_1^2)^{1/2}} \right|, \tag{20}$$

$$I_3^{(jt)} = \left| \frac{1}{(d^2+s_1^2)^{1/2}} - \frac{1}{(d^2+s_2^2)^{1/2}} \right|, \tag{21}$$

$$I_4^{(jt)} = \left| I_1^{(jt)} + \frac{s_1}{(d^2+s_1^2)^{1/2}} - \frac{s_2}{(d^2+s_2^2)^{1/2}} \right|. \tag{22}$$

Case II : $\alpha \geq \left\|\mathbf{x}_b^{(jt)} - \mathbf{x}_a^{(jt)}\right\|$.

The same integration limits and expressions in case I above are obtained, except for $I_3^{(jt)}$, here given by

$$I_3^{(jt)} = - \left| \frac{1}{(d^2+s_1^2)^{1/2}} - \frac{1}{(d^2+s_2^2)^{1/2}} \right|. \tag{23}$$

Case III : $0 < \alpha < \left\|\mathbf{x}_b^{(jt)} - \mathbf{x}_a^{(jt)}\right\|$.

In this case, $s_1 = l_1$, $s_2 = l_2$, while l_1 and l_2 are given by relations (18), and the following expressions result:

$$\begin{aligned} I_1^{(jt)} &= \ln[(d^2+s_1^2)^{1/2} + s_1] + \ln[(d^2+s_2^2)^{1/2} + s_2] \\ &\quad - 2\ln(d), \end{aligned} \tag{24}$$

$$I_2^{(jt)} = \frac{1}{d^2} \left[\frac{s_2}{(d^2+s_2^2)^{1/2}} + \frac{s_1}{(d^2+s_1^2)^{1/2}} \right], \tag{25}$$

$$I_3^{(jt)} = \left[\frac{1}{(d^2+s_1^2)^{1/2}} - \frac{1}{(d^2+s_2^2)^{1/2}} \right], \tag{26}$$

$$I_4^{(jt)} = \left| I_1^{(jt)} - \left[\frac{s_1}{(d^2+s_1^2)^{1/2}} + \frac{s_2}{(d^2+s_2^2)^{1/2}} \right] \right|. \tag{27}$$

The 1D quadrature that employs the analytical expressions for computing A_l and B_{lkm}, relations (11) and (12) (associated with the strongly singular kernels) will be denoted by $^{cl}L^{(1)}(m)$, where m is the number of integration points adopted for evaluating the solid angle, $\Phi^{(\xi,e)}$; regular numerical quadratures can be conveniently applied for this integral. Note that the complete quadratures based on the line-integral approach, which include surface and line integrals, will be denoted by either $[L^{(2)}(n_1,n_2), \ ^{num}L^{(1)}(m)]$ or $[L^{(2)}(n_1,n_2), \ ^{cl}L^{(1)}(m)]$.

2.1.3 Integration tests

Araújo and Gray (2008) demonstrated the efficiency of the $[L^{(2)}(n_1,n_2), \ ^{num}L^{(1)}(m)]$ quadrature. To see the improvement brought about by analytically computing the nearly-strongly-singular integrals, both line-integral approaches discussed previously are employed to calculate the diagonal-block terms of the **H** matrix resulting from modeling the cube shown in Fig. 3. In

this test the side length is $a = 1$ and discontinuous boundary elements, generated by displacing the nodes of $d = 5.0 \times 10^{-5}$ at all its surfaces, are used. The coefficient values evaluated by employing the two different line-integral approaches are contrasted with high-precision values calculated by the combined coordinate-transformation-based quadrature with 20×20 integration points and 20 integration subelements. $L^{(2)}(n_1, n_2)$ quadratures with $n_1 = n_2 = 6$, 8, and 10 are employed for the quasi-singular surface integrals. As virtually no difference is observed for these different integration orders, only results for $n_1 = n_2 = 6$are shown in Fig. 4. This shows that the quadrature based on the combined coordinate transformation is appropriate for calculating these surface integrals. For the numerical evaluation of the line integrals, integration points varying from $m = 5$ to $m = 100$ are adopted. As one sees from Fig. 4(a), integration convergence for the diagonal terms, $c_{ii} + h_{ii}$, is already attained with 5 integration points employing either $^{num}L^{(1)}$ and $^{cl}L^{(1)}$ quadratures. However, for the off-diagonal terms, $c_{ij} + h_{ij}, i \neq j$, a high number of integration points ($m \geq 20$) is needed for the $^{num}L^{(1)}$quadrature to converge. Even for $m = 40$, the diagonal block matrices are not symmetric. On the other hand, the $^{cl}L^{(1)}$ procedure has already converged to the high-precision values with 5 integration points. Moreover, if no polynomial transformation is applied to derive $^{num}L^{(1)}$, unacceptable $c_{ij} + h_{ij}$ values are obtained for $d = 5.0 \times 10^{-5}$, even with $m = 100$. Based on these partial results, one can conclude that employing analytical expressions substantially increases the efficiency of the integral-line approach. Therefore, in the applications later in this paper, only $^{cl}L^{(1)}$-based quadratures are considered along with the line-integral approach.

2.2 Subregion-by-subregion technique applied to solids with repeated parts

To have insight into the micromechanics of composites that consist of fibers scattered in a material matrix (see Fig. 5), the analysis method must have the ability to effectively model the many parts of this coupled, sometimes multi-
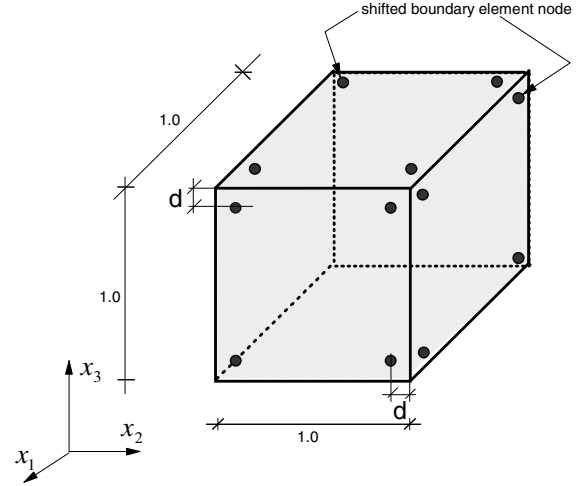

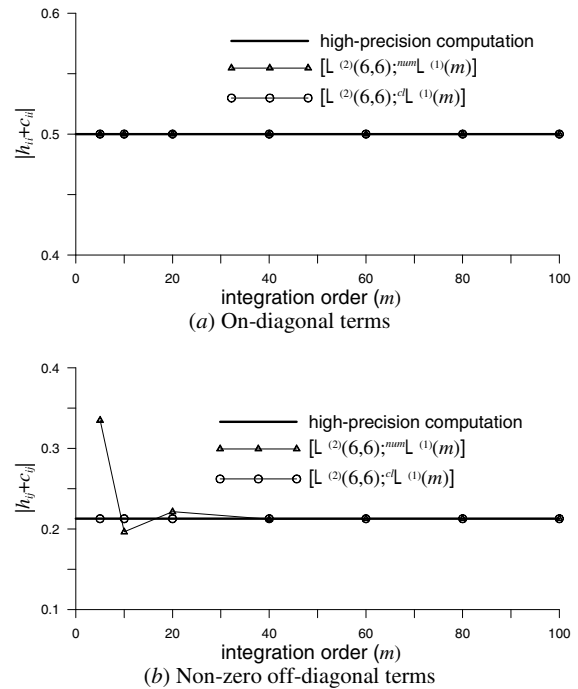Figure 3: Cube with discontinuous boundary elements

Figure 4: **H** diagonal-block coefficients ($d = 5.0 \times 10^{-5}$)

scale, physical system. For example, the composite could consist of many thin-walled reinforcing fibers and void spaces. Here, the subregion-by-subregion technique proposed in Araújo, Silva, and Telles (2006) is employed to model this type

of composite. This technique is similar to the element-by-element technique, widely applied to solve large-scale engineering problems with finite elements (FEM) [Hughes, Levit, and Winget (1983); Hughes, Ferencz, and Hallquist (1987); Fried (1994)]. Its main idea is to use an iterative solver. This allows working with smaller parts of the system of equations without explicitly assembling the global matrix. As a consequence of overlapping coefficients in the FEM stiffness matrices, edge-based data structures have been employed to minimize CPU time and memory requirements [Coutinho, Martins, Sydenstricker, and Elias (2006); Elias, Martins, and Coutinho (2006)]. By contrast, in the boundary-element subregion-by-subregion technique (SBS), no further data-structure optimization is needed, as coefficients belonging to edges shared by different subregions do not overlap.

For n_s subregions, after introducing the boundary conditions, the BE global system of equations can be written as

$$\sum_{m=1}^{i-1} (\mathbf{H}_{im}\mathbf{u}_{mi} - \mathbf{G}_{im}\mathbf{p}_{im}) + \mathbf{A}_{ii}\mathbf{x}_i$$
$$+ \sum_{m=i+1}^{n} (\mathbf{H}_{im}\mathbf{u}_{im} + \mathbf{G}_{im}\mathbf{p}_{mi}) = \mathbf{B}_{ii}\mathbf{y}_i, \quad i = 1, n_s,$$

(28)

where $\mathbf{H}_{ij}$ and $\mathbf{G}_{ij}$ denote the usual BE matrices obtained for source points pertaining to subregion Ω_i and associated respectively with the boundary vectors $\mathbf{u}_{ij}$ and $\mathbf{p}_{ij}$ at Γ_{ij}. Note that if $i \neq j$, Γ_{ij} corresponds to the interface between Ω_i and Ω_j; Γ_{ii} is the outer boundary of Ω_i.

In the SBS data structure, the subsystems in Eq. (28) are then separately stored and manipulated. Thus, the many zero blocks, unavoidably present in the global system matrix, are completely excluded. Moreover, as discontinuous boundary elements are employed, the fiber-matrix perfect bonding interfacial conditions, given by

$$\begin{cases} \mathbf{u}_{ij} = \mathbf{u}_{ji} \\ \mathbf{p}_{ij} = -\mathbf{p}_{ji} \end{cases}, \quad \text{at } \Gamma_{ij}$$

(29)

can be imposed pairwise. This enormously simplifies the treatment of edges and corners at subregion interfaces.
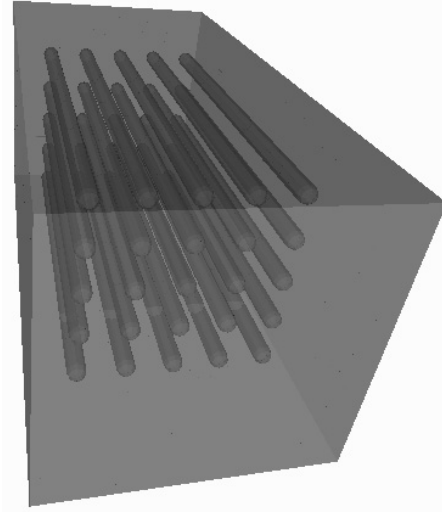

Figure 5: Fiber-reinforced composite

In previous works, both *unstructured* (UNSMVP) and *structured matrix-vector products* (SMVP) have been employed [see Araújo, Silva, and Telles (2006); Araújo and Gray (2008)]. In the latter procedure, the matrix columns of a given subregion are re-ordered so as to group its coefficients into three separate blocks: one associated with interfaces Γ_{ij} for which $i > j$, a second associated with the outer boundary Γ_{ii}, at which boundary values are prescribed, and one associated with interfaces Γ_{ij} for $i < j$. One works then with the following data structure for matrices $\mathbf{H}_i$ and $\mathbf{G}_i$, for the i-*th* subregion:

$$\begin{aligned} \mathbf{H}_i &= [\ \overbrace{\mathbf{H}_{i1} \ldots \mathbf{H}_{i,i-1}}^{\text{block 1}} \ \overbrace{\mathbf{H}_{ii}}^{\text{block 2}} \ \overbrace{\mathbf{H}_{i,i+1} \ldots \mathbf{H}_{i,n}}^{\text{block 3}} \ ] \\ \mathbf{G}_i &= [\ \ \mathbf{G}_{i1} \ldots \mathbf{G}_{i,i-1} \ \ \ \mathbf{G}_{ii} \ \ \ \mathbf{G}_{i,i+1} \ldots \mathbf{G}_{i,n} \ \ ] \end{aligned}$$

(30)

This data structure is precisely that indicated in Eq. (28), and it has been shown to improve the efficiency of the iterative solver [Araújo and Gray (2008)].

The Jacobi-preconditioned BiCG solver (J-BiCG) [Mansur, Araújo, and Malaghini (1992)] is adopted in this study. In this algorithm, matrix-vector products of the form $(\mathbf{D}^{-1}\mathbf{A})\mathbf{p}_j$ and $(\mathbf{D}^{-1}\mathbf{A})^T\mathbf{p}_j^*$ are computed, where $\mathbf{A}$ and $\mathbf{D}$ are,

respectively, the global matrix of the coupled system and its diagonal matrix. Nevertheless, other Krylov solvers can also be implemented along with the SBS technique; recent advances in Krylov solvers for non-hermitian matrices are reported in Saad (2003), and van der Vorst (2003).

In conjunction with the SBS technique, a "matrix-copy" option is particularly important for modeling fiber composites containing physically and geometrically identical reinforcement elements. In this approach, the BE matrix is assembled for only one substructure, and for the other repeated substructures, the corresponding matrix is promptly obtained by rotation transformations. Matrix-assembly CPU time is then considerably reduced.

3 Evaluating effective material parameters

For understanding fiber-reinforced composite structures on the macromechanical scale, an essential step is the material characterization on the micromechanical level. In this paper, square-packed and hexagonal-packed arrays are considered to idealize the smearing of fibers inside the matrix material (see Fig. 6). The boundary-element SBS technique discussed above is applied to analyze the 3D material specimens, representative volume elements - RVE. Long and short fibers are considered as well as models consisting of a single or several unit cells. Based on the evaluation of displacements and stresses on the boundary of the specimens for germane loading cases, the macroscopic material constants can be evaluated. In Fig. 6, the unit cells for both fiber-array patterns [Hyer (1998)] are depicted, and in Fig. 7 the details of single-cell specimens for long-fiber-based composites are shown. For comparison purposes, rules of mixture, based on the fiber volume fraction, will also be considered in this study to estimate effective elasticity moduli.

3.1 Constants E_1, υ_{12} and υ_{13}

For these constants, one considers the specimen under stretching (or shortening) in the 1 principal material direction (fiber direction), and boundary conditions on the lateral surfaces perpendicular to the 2 and 3 directions are imposed to sim-
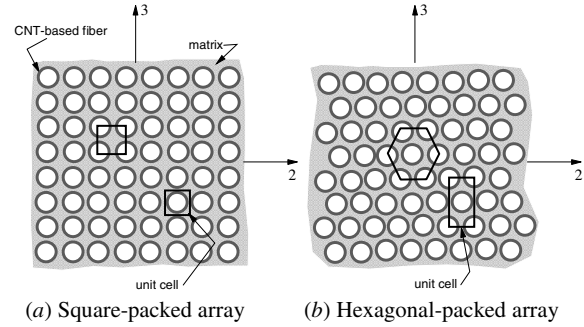

(*a*) Square-packed array   (*b*) Hexagonal-packed array

Figure 6: Fiber-packing patterns

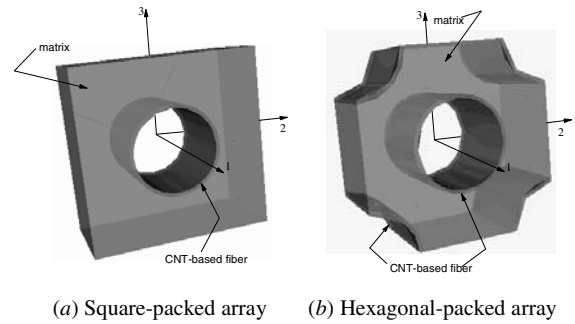(*a*) Square-packed array   (*b*) Hexagonal-packed array

Figure 7: Single-cell composite specimens

ulate the surrounding medium. Following Hyer (1998), these *in-situ* boundary conditions may be enforced by allowing the lateral surfaces of the specimen to move freely and to change length as long as they remain straight and free of any net force. Although an iterative algorithm may be designed to exactly enforce these boundary conditions, herein a simpler strategy is adopted. First, the solution is obtained for a prescribed axial displacement $\overline{\delta}_1^{(1)}$ and the corresponding transverse displacements, $\delta_2^{(1)}$ and $\delta_3^{(1)}$, are computed. A second analysis is then carried out with the displacements $\overline{\delta}_1^{(1)}$ and $\overline{\delta}_2^{(1)} = \overline{\delta}_3^{(1)} = \overline{\delta}_t^{(1)}$ as prescribed data, where $\overline{\delta}_t^{(1)}$ is a mean lateral displacement value (see Fig. 8).

Note that imposing $\overline{\delta}_2^{(1)} = \overline{\delta}_3^{(1)}$ is appropriate, as transverse isotropy applies to the fiber-packed arrays being considered. In addition, the minimum and maximum transverse displacements at the lateral surfaces of the RVE are in general about the
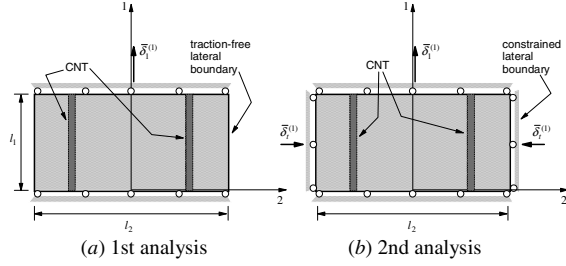
Figure 8: Boundary conditions in strain state 1

same value; thus a more sophisticated method for enforcing the zero-force condition is not required. The overbar notation $\overline{\delta}$ indicates prescribed displacement, and the superscripts stand for strain state 1, from which the material parameters E_1, υ_{12} and υ_{13} are determined. The following expressions, derived from basic strain-stress relationships, are employed for this purpose:

$$E_1 = \left(\overline{\sigma}_1^{(1)} - \upsilon_{12}\overline{\sigma}_2^{(1)} - \upsilon_{13}\overline{\sigma}_3^{(1)} \right) \left(\frac{l_1}{\overline{\delta}_1^{(1)}} \right), \quad (31)$$

$$\nu_{12} = \nu_{13} = - \left(\frac{\overline{\delta}_2^{(1)}}{l_2} \right) \left(\frac{l_1}{\overline{\delta}_1^{(1)}} \right), \quad (32)$$

where $\overline{\sigma}_i^{(1)}$ denotes the average stress over the corresponding RVE area. In the (approximate) calculations the net forces on the lateral surfaces are not exactly zero; thus $\overline{\sigma}_2^{(1)}$ and $\overline{\sigma}_3^{(1)}$ are retained in Eq. (31).

3.2   Constants E_2, υ_{23} and υ_{21}

For evaluating these constants, we employ the strain state 2 shown in Fig. 9, in which $\overline{\sigma}_1^{(2)} = 0$. In this case, the minimum and maximum values of the transverse displacement on the 3 surface of the specimen, $\delta_3^{(2)}$, may be substantially different. Thus, compared to the analysis for strain state 1, a more elaborated method is needed for finding the $\overline{\delta}_3^{(2)}$ value associated with a zero net force condition on that surface, $f_3^{(2)} = 0$ (in-situ boundary conditions). Again, a first analysis is carried out for a prescribed lateral displacement $\overline{\delta}_2^{(2)}$, and $\delta_3^{(2)}$ is determined. Assuming a linear variation

for $f_3^{(2)}$ (the net force resultant) as a function of prescribed values $\tilde{\delta}_3^{(2)}$ on the 3 surface (see Fig. 10), $\overline{\delta}_3^{(2)}$ is determined by

$$\overline{\delta}_3^{(2)} = {}^{(b)}\tilde{\delta}_3^{(2)} - \left(\frac{{}^{(b)}\tilde{\delta}_3^{(2)} - {}^{(a)}\tilde{\delta}_3^{(2)}}{{}^{(b)}f_3^{(2)} - {}^{(a)}f_3^{(2)}} \right)^{(b)} f_3^{(2)}. \quad (33)$$
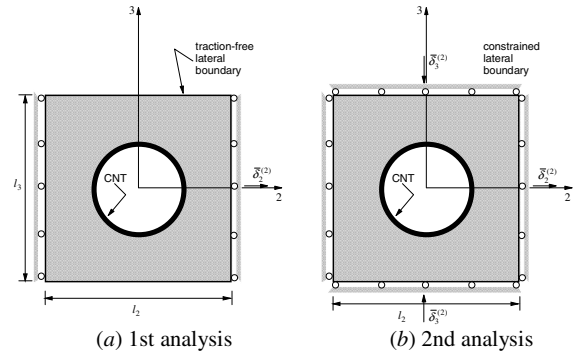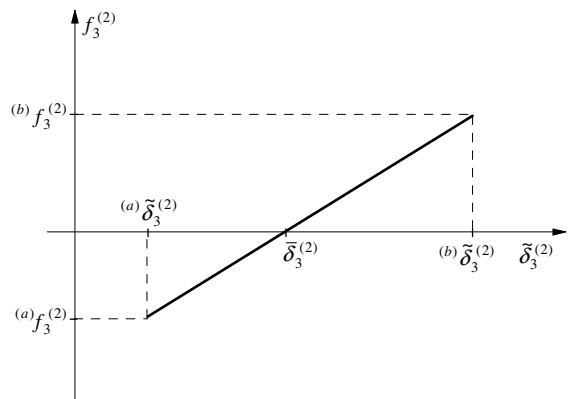

Figure 9: Boundary conditions in strain state 2

Figure 10: Net force variation of $f_3^{(2)}$

Then, by taking $\overline{\delta}_2^{(2)}$ and $\overline{\delta}_3^{(2)}$ as boundary condition, an additional analysis is carried out, from which E_2, υ_{23} and υ_{21} are calculated. Here, the following expressions are employed for calculat-

ing these constants:

$$E_2 = \left(\overline{\sigma}_2^{(2)} - \upsilon_{23}\overline{\sigma}_3^{(2)}\right)\left(\frac{\overline{\delta}_2^{(2)}}{l_2}\right)^{-1}, \qquad (34)$$

$$\upsilon_{23} = -\left(\frac{\overline{\delta}_3^{(2)}}{l3}\right)\left(\frac{l_2}{\overline{\delta}_2^{(2)}}\right), \qquad (35)$$

$$\upsilon_{21} = \upsilon_{12}\left(\frac{E_2}{E_1}\right), \qquad (36)$$

where the average stress $\overline{\sigma}_3^{(2)}$ is approximately null. More precise strategies for finding $\overline{\delta}_3^{(2)}$, such as non-linear interpolations or, as already mentioned, iterative procedures, can also be easily developed.

Of course, assuming transverse isotropy in the 2-3 plane, the shear modulus G_{23} is directly calculated from the constants above by

$$G_{23} = \frac{1}{2}\left(\frac{E_2}{1 + \upsilon_{23}}\right), \qquad (37)$$

Note that, in case of fully orthotropic materials, a third strain state similar to strain state 2 (but with some $\overline{\delta}_3^{(3)}$ initially prescribed) can be employed to evaluate E_3, υ_{31} and υ_{32}.

3.3 Rules of mixture

For comparison purposes, rules of mixture based on the fiber volume fraction, V_f, have been employed to estimate the elasticity modulus of the composite specimens. Particularly for intervals with constant V_f, as for the 1 direction of RVEs with CNT-based fibers across their whole length l_1, the effective elasticity modulus can be approximated by [Hyer (1998); Chen and Liu (2004)]

$$E_1 = E_f V_f + E_m(1 - V_f), \qquad (38)$$

where E_f and E_m are respectively the fiber and the matrix elasticity modulus. Note that the fiber volume fraction for CNT square-packed ($V_f^{(sq)}$) and hexagonal-packed ($V_f^{(hex)}$) arrays are given by

$$V_f^{(sq)} = \frac{\pi\left(r_0^2 - r_i^2\right)}{\left(l_2 l_3 - \pi r_i^2\right)}$$
$$V_f^{(hex)} = \frac{2\pi\left(r_0^2 - r_i^2\right)}{\left(l_2 l_3 - 2\pi r_i^2\right)} \qquad (39)$$

r_0 and r_i being, respectively, the outer and inner radius of the nanotube.

For short CNTs (see Fig. 11) wherein the fiber volume fraction is no longer constant along the entire length l_1, an expression for E_1 can be obtained from the stress-strain relationship for a one-dimensional rod under axial load. This assumes that the rod is composed of two parts, one of length l_e consisting of pure matrix material, and one of length l_c containing polymer matrix and CNT at some constant volume fraction V_f [Chen and Liu (2004)]. One has

$$E_1 = \left[\left(\frac{1}{E_m}\right)\left(\frac{l_e}{l}\right) + \left(\frac{1}{E_1^c}\right)\left(\frac{l_c}{l}\right)\left(\frac{A}{A_c}\right)\right]^{-1}, \qquad (40)$$

with $l = l_c + l_e$, $A_c = l_2 l_3 - \pi r_i^2$ for square-packed arrays, $A_c = l_2 l_3 - 2\pi r_i^2$ for hexagonal-packed arrays, and E_1^c, the effective elasticity modulus of the central part of the composite, calculated according to expression (38).
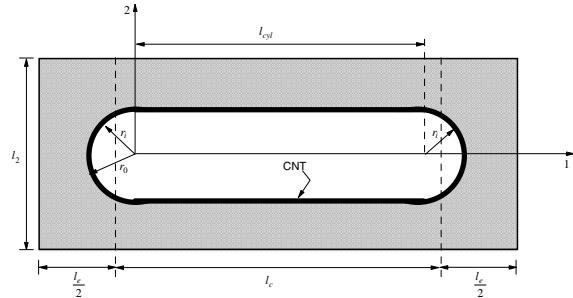

Figure 11: Short CNT inside the matrix

Note that the fiber volume fraction along the caps is variable. Thus, it is reasonable to define l_c as some value in the interval $[l_{cyl}, l_{cyl} + 2r_0]$, where l_{cyl} is the length of the central cylinder (see Fig. 11). Chen and Liu (2004) consider $l_c = l_{cyl} + 2r_0$.

4 Applications and discussions

The BE SBS technique, together with the new integration procedures and matrix-copy option, has been applied to evaluate engineering constants

for several CNT-based composites. In the numerical tests, long and short CNTs distributed in square-packed and hexagonal-packed arrays inside a matrix material form the composite specimens (RVEs). Single-unit-cell and multi-unit-cell specimens are considered. The quadratures $[L^{(2)}(8,8),\ ^{cl}L^{(1)}(6)]$, employing closed expressions for the nearly-strongly-singular line integrals, have been applied in all problems. For comparison purposes, the physical constants adopted by Chen and Liu (2004) for the CNT and polymer matrix are considered for all the calculations in this paper:

CNT:

$$E_{CNT} = 1,000\,nN/nm^2(GPa); \quad v_{CNT} = 0.30,$$

Matrix:

$$E_m = 100\,nN/nm^2(GPa); \quad v_{CNT} = 0.30.$$

The cylindrical cross section and, when present, the hemispherical caps of the CNT fibers have outer radius $r_0 = 5.0\,nm$ and inner radius $r_i = 4.6\,nm$. Discontinuous boundary elements, when needed, are generated by shifting the nodes interior to the elements a distance of $d = 0.10$ (measured in natural coordinates). Common to all analyses is the quadratic boundary element adopted, an 8-node quadrilateral boundary element, and the tolerance for the iterative solver (J-BiCG), taken as $\zeta = 10^{-6}$.

4.1 Square-packed long CNT arrays

RVEs based on a single, 2×2, and 3×3 unit cells are employed for modeling long-CNT-reinforced composites. For the long-fiber-reinforced composites, the observed response does not vary along the fiber direction (1 direction) of the specimen, and thus, any convenient length l_1 [see Figs. 7(a), 8(a)] can be taken. In the analyses here, $l_1 = 10\,nm$, which allows a single layer of boundary elements across the fiber (see BE models below).

4.1.1 Single-unit-cell-based RVE

This RVE has dimensions $l_1 = 10\,nm$, and $l_2 = l_3 = 20\,nm$. In the BE model in Fig. 12, two

subregions are considered: one for the matrix material, one for the CNT. Both the matrix material and the CNT are modeled with 64 boundary elements, resulting in a total of 1,824 degrees of freedom for the global system. Discontinuous boundary elements are placed on the interface between the matrix material and the carbon nanotube. By solving this RVE with the loading cases described in section 3 (strain state 1 and 2) and applying expressions 31-32 and 34-35, the engineering constants shown in Tab. 1 are calculated. The rule-of-mixture estimate (Eq. 38) furnishes $E_1/E_m = 1.3255$, where the fiber volume fraction is $V_f = 3.617\%$.
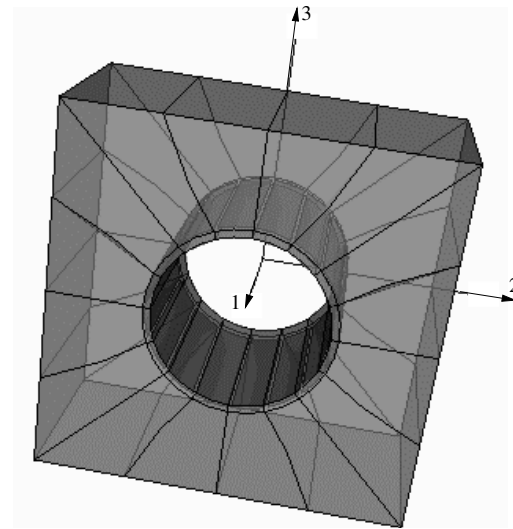

Figure 12: BE model for single-unit-cell RVE for long CNT square-packed arrays

Table 1: Engineering constants for single-unit-cell RVEs (long CNT, square-packed array)

	Chen & Liu (3D FE)	BE SBS
E_1/E_m	1.3255	1.3227
$E_2/E_m, E_3/E_m$	0.8492	0.8323
v_{12}, v_{13}	0.3000	0.2974
v_{23}	0.3799	0.3757

As one sees, good agreement with the values estimated according to the rule of mixture, and those obtained by Chen and Liu (2004) using refined 3D

FE models, is achieved. It should also be noted that the n_{it}/n values, where n_{it} is the number of iterations for the solver and n the system order (n=1824), indicate good solver performance for both loading cases; these numbers were 0.28 for strain state 1 and 0.25 for strain state 2. The sparsity of the global matrices is 29% in both cases.

4.1.2 2×2- and 3×3- *unit-cell RVE*

To confirm that single-unit-cell RVEs produce accurate results, RVEs containing 2×2 and 3×3 unit cells have also been analyzed (see Figs. 13 and 14). Each cell has the same geometry of that in Fig. 12 above. One subregion for the matrix material and one for each CNT is considered. For the CNTs, the BE matrix is only assembled for one, and as explained above, copied for the others. For the models with 2×2 and 3×3 unit cells the global systems have 6,990 15,504 equations, the matrix material having been modeled with 224 elements (666 nodes) and 480 elements (1,424 nodes) respectively. As before, each CNT has 64 elements (192 nodes), and discontinuous elements are employed at the polymer-CNT interfaces.
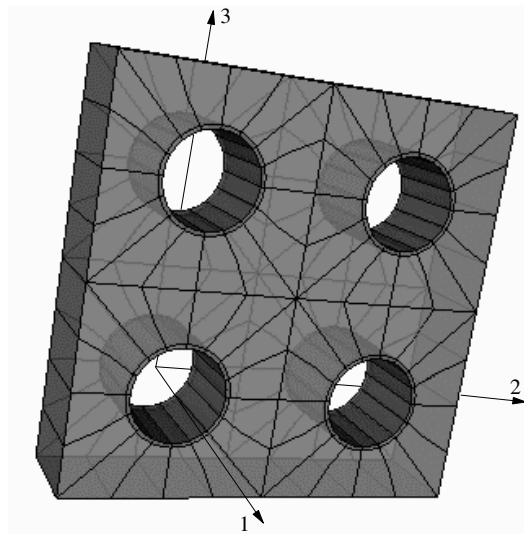

Figure 13: BE model for 2×2-unit-cell RVE for long CNT square-packed arrays
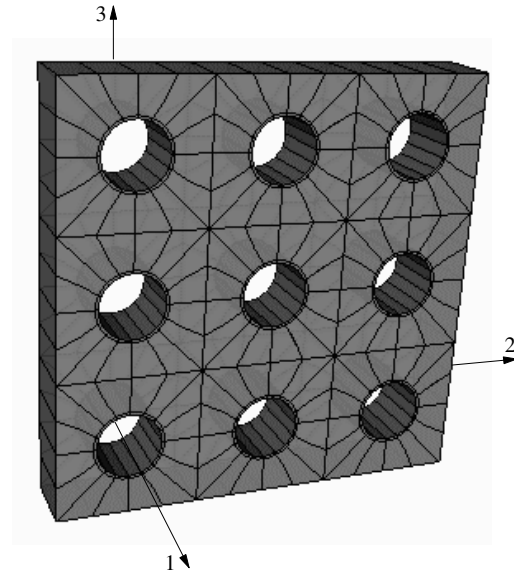
In Tabs. 2 and 3, the composite elastic con-

Figure 14: BE model for 3×3-unit-cell RVE for long CNT square-packed arrays

stants calculated employing these RVEs are presented. No considerable changes are observed in these values, which indicates that, for the determination of elastic constants, single-unit-cell-based RVEs satisfactorily represent the composite material. Moreover, these calculations highlight the computational efficiency of the matrix-copy option in case of repeated substructures. The n_{it}/n values once again indicate good solver performance. For the 2×2-cell RVE, these values are 0.21 in the strain state case 1 and 0.19 in the strain state case 2. For the 3×3-cell RVE, n_{it}/n =0.24 and n_{it}/n =0.21 in the respective strain state cases 1 and 2. The global matrix sparsity for the model in Fig. 13 (with 5 subregions) is 57% and for the model in Fig. 14 (with 10 subregions), 63%. It should be noted that the higher the sparsity, the less the relative CPU time per iteration.

4.2 *Hexagonal–packed long CNT arrays*

For hexagonal packing of fibers, single-cell and 2×2-cell RVEs have been considered. Again, $l_1 = 10$ *nm* and $l_2 = l_3 = 20$ *nm* for each unit cell (see Figs. 7, 8, and 9 for definitions of l_1, l_2, and l_3). The RVEs are modeled with 6 and 14 sub-

Table 2: Engineering constants for 2×2-unit-cell RVEs (long CNT, square-packed array)

	Chen & Liu (3D FE)	BE SBS
E_1/E_m	1.3255	1.3225
$E_2/E_m, E_3/E_m$	0.8492	0.8319
v_{12}, v_{13}	0.3000	0.2975
v_{23}	0.3799	0.3597

Table 3: Engineering constants for 3×3-unit-cell RVEs (long CNT, square-packed array)

	Chen & Liu (3D FE)	BE SBS
E_1/E_m	1.3255	1.3225
$E_2/E_m, E_3/E_m$	0.8492	0.8319
v_{12}, v_{13}	0.3000	0.2975
v_{23}	0.3799	0.3597

regions, see Figs. 15 and 16. The BE models for the subregions in Fig. 15 have the following characteristics: 64 elements (192 nodes) for the matrix material and central CNT, and 10 elements (32 nodes) for each quarter CNT, giving a total of 2,568 degrees of freedom. The model in Fig. 16 has 240 elements (712 nodes) for the matrix, 32 elements (96 nodes) for the central CNT, 64 elements (192 nodes) for the other CNTs, 18 elements (56 nodes) for the half CNTs, and 10 elements (32 nodes) for the quarter CNTs, resulting in a total of 9,864 equations. At all matrix-CNT interfaces, discontinuous elements are employed. The material parameters obtained for this packing-array pattern are show in Tabs. 4 and 5. Here, a comparison was possible only for E_1, estimated through Eq. 38 for a fiber volume fraction $V_f = 9.035\%$. Computational performance parameters are: for the single-cell model, n_{it}/n= 0.14 in strain states 1 and 2; for the 2×2-cell model, n_{it}/n=0.08 also in both strain states (1 and 2). These values again indicate very good solver performance. The sparsity of the models is 53% for the model in Fig. 15, and 66% for the one in Fig. 16.

4.3 *Square-packed short CNT arrays*

Short capsule-like CNTs as those shown in the BE models in Figs. 17 and 18 can also be used
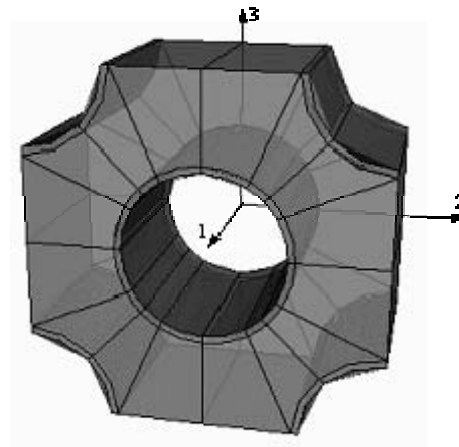

Figure 15: BE model for single-unit-cell RVE, long CNT, hexagonal-packed array
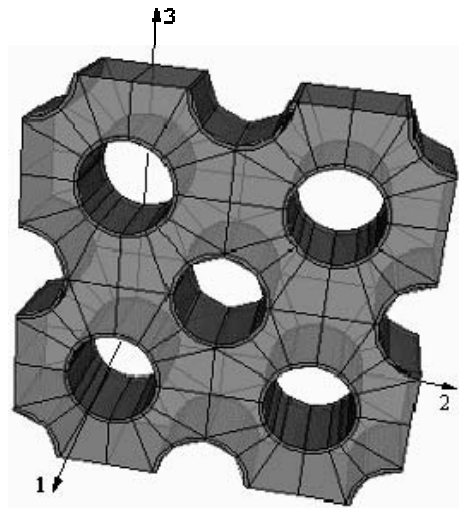

Figure 16: BE model for 2×2-unit-cell RVEs (long CNT, hexagonal-packed array)

Table 4: Engineering constants for single-unit-cell RVEs (long CNT, hexagonal-packed array)

	BE SBS	Rules of mixture
E_1/E_m	1.8081	1.8131
$E_2/E_m, E_3/E_m$	1.0889	-
v_{12}, v_{13}	0.2943	-
v_{23}	0.5106	-

as reinforcement. The single-cell representative volume element in Fig. 17 has been analyzed in

Table 5: Engineering constants for 2×2-unit-cell RVEs (long CNT, hexagonal-packed array)

	BE SBS	Rule of mixture
E_1/E_m	1.8067	1.8131
$E_2/E_m, E_3/E_m$	1.0839	-
v_{12}, v_{13}	0.2932	-
v_{23}	0.5103	-

Chen and Liu (2004). The outer dimensions of the RVE in Fig. 17 are $l_1 = 100 \, nm$, and $l_2 = l_3 = 20 \, nm$. The CNT is 50 nm long (including the hemispherical caps), and the radii of its cylindrical part and hemispherical caps are $r_0 = 5.0 \, nm$ and $r_i = 4.6 \, nm$. The model in Fig. 17 contains two subregions, one for the matrix and one for the CNT. The BE mesh for the matrix has 192 elements (580 nodes), and for the CNT, 160 elements (484 nodes), giving a total of 3192 degrees of freedom for the global model. Note that discontinuous elements are not needed here, as all the interfaces are smooth and the boundary conditions can also be imposed employing continuous elements. The model in Fig. 18, with 5 subregions, has 2×2 unit cells, each one with the same characteristics of that in Fig. 17. The BE matrices for the CNTs are again calculated using the matrix-copy option, i.e. only one matrix is in fact calculated. A multi-cell model is also employed to verify the performance of the single-cell results for the composite material. The results from these analyses contrasted with results obtained by Chen and Liu (2004) are shown in Tabs. 6 and 7. The corresponding estimates for E_1 based on the rule of mixture for short-fiber composite (Eq. 40 with $E_1^c = 132.553 \, nN/nm^2$) yield $E_1/E_m = 1.0396$ (with $l_c = 40 \, nm$ and $l_e = 60 \, nm$), and $E_1/E_m = 1.0500$ with $l_c = l_e = 50 \, nm$.

Table 6: Engineering constants for single-unit-cell RVEs (short CNT, square-packed array)

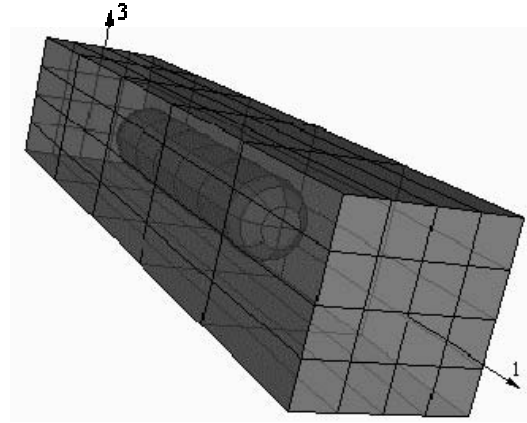|	Chen & Liu (3D FE)	BE SBS
E_1/E_m	1.0391	1.0378
$E_2/E_m, E_3/E_m$	0.9342	0.9366
v_{12}, v_{13}	0.3009	0.2963
v_{23}	0.3217	0.3207

Figure 17: BE model for single-unit-cell RVE for square-packed short-CNT array
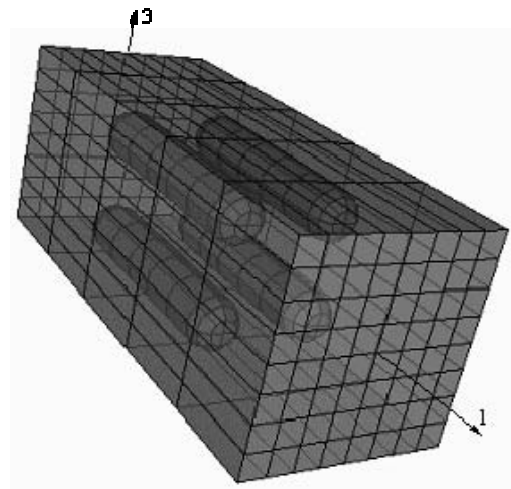

Figure 18: BE model for 2×2-unit-cell RVE, short CNT, square-packed array

Table 7: Engineering constants for 2×2-unit-cell RVEs (short CNT, square-packed array)

	Chen & Liu (3D FE)	BE SBS
E_1/E_m	1.0391	1.0378
$E_2/E_m, E_3/E_m$	0.9342	0.9366
v_{12}, v_{13}	0.3009	0.2978
v_{23}	0.3217	0.3206

The present results show very good agreement with numbers obtained by Chen and Liu (2004) employing a refined finite-element mesh. The

n_{it}/n relations also indicate very good convergence rates: for the model in Fig. 17, 0.18 and 0.20 for strain state 1 and 2 respectively, and for the model in Fig. 18, 0.14 for strain state 1 and 0.14 for strain state 2. The sparsity of the global matrices is 27% for the single-cell RVE, and 54% for the 2×2-cell RVE. It should be especially noted that boundary element meshes for 2×2-cell RVE are easily constructed.

4.4 Hexagonal-packed short CNT arrays

In this application, a single-unit-cell RVE based on the hexagonal-packing array is considered (Fig. 18). The RVE is modeled with 6 subregions: one for the matrix, one for the central CNT, and 4 for the quarter CNTs. In this case the matrix-copy option is not exploited. The boundary elements on the interfaces between the quarter CNTs and the matrix are discontinuous. The BE subregion for the matrix has 384 elements (1156 nodes), that for the central CNT 160 elements (484 nodes), and that for each quarter CNT 50 elements (152 nodes). The global system, after discontinuous elements are generated, has 9,072 equations.
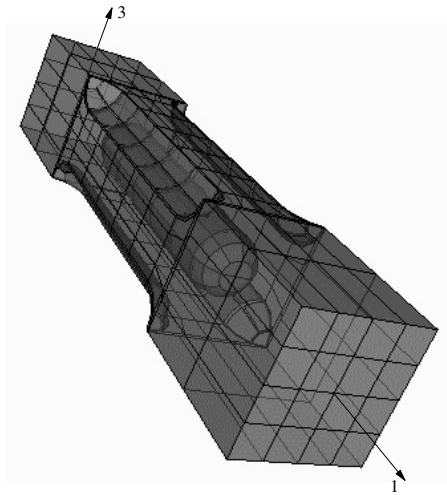

Figure 19: BE model for single-unit-cell RVEs (short CNT, hexagonal-packed array)

The effective material constants for the CNT-array pattern are given in Tab. 8. Here, the value for E_1 is compared with the value calculated from

Eq. 40 with $E_1^c = 181.315 \ nN/nm^2$ and $l_c = 40$ nm and $l_e = 60 \ nm$; this is more realistic than that calculated by taking $l_c = l_e = 50 \ nm$, as the load transmission is brought about mainly through the cylindrical lateral surface of the CNT. The sparsity of the global matrix is 53%, and n_{it}/n values are 0.11 for both strain states 1 and 2, indicating very good solver performance. It is again emphasized that, by avoiding domain discretization, the BE models are easily generated.

All the problems above have also been analyzed for solver tolerance $\zeta = 10^{-8}$. In this case, the number of iterations, n_{it}, just increased for no virtual modification in the calculated material properties. Thus, the corresponding results have not been shown.

Table 8: Engineering constants for single-unit-cell RVE, short CNT, hexagonal-packed array

	BE SBS	Rule of mixture
E_1/E_m	1.0777	1.0748
$E_2/E_m, E_3/E_m$	1.0878	-
v_{12}, v_{13}	0.2953	-
v_{23}	0.3621	-

5 Conclusions

A 3D linear elasticity boundary-element formulation based upon a robust subregion-by-subregion (SBS) technique has been developed, and subsequently applied to evaluate effective engineering constants for CNT-reinforced composites. Moreover, the efficiency of the line-integral approach for evaluating weakly-singular and strongly-singular integrals has been substantially improved by incorporating analytical integrations. Numerical tests of these procedures have shown excellent convergence for relatively few Gauss points, even for source points as close as $d = 5.0 \times 10^{-5}$ to element edges; by contrast, direct numerical evaluation of the nearly-strongly-singular line integrals requires a large number of integration points ($m \geq 20$) to obtain accurate **H** coefficients.

An important consequence of the improved quadrature algorithms is that this greatly simpli-

fies the meshing constraints for modeling composites. Disproportionate boundary elements can be employed without sacrificing accuracy, and as demonstrated herein, relatively coarse meshes can be used to model thin-walled solids (e.g., CNTs). Moreover, efficient quasi-singular integration also allows the reliable use of discontinuous boundary elements, providing a relatively simple strategy for modeling complex coupled domains by means of the SBS algorithm.

As demonstrated by the numerical results, the techniques discussed have proven to be very convenient for analyzing representative volume elements of CNT-reinforced composites. In addition to the special quadratures, the matrix-copy option also increases the efficiency of the BE algorithm, avoiding the repeated calculation of matrices for identical substructures. This significantly reduces the total matrix-assembly time, while the J-BiCG iterative solver has also shown very good performance for these problems: for a stopping criterion of $\zeta = 10^{-6}$, $n_{it}/n <0.20$ for most of the analyses. Moreover, BiCG variants such as the BiCGSTAB(l) [Sleijpen and Fokkema (1993)] and the GPBiCG [Zhang (2002)], capable of higher convergence rates than the pure BiCG, should be incorporated into the next version of the SBS algorithm.

The fact that a smaller tolerance for the iterative solver produced virtually no change in the solution raises an interesting question, namely how to choose when to halt the iterations. Clearly, too few may lead to a poor solution, while too many iterations just waste CPU time without improving accuracy. An effective stopping criterion is an essential issue in using any iterative solvers, and is especially important for mixed boundary data in elasticity calculations. In this situation, the values of the displacement and traction unknowns are usually quite disparate, and this may cause some problems for iterative solvers.

As a final comment regarding efficiency, note that the SBS approach effectively exploits the sparsity of the global system, the memory required and the CPU time per iteration are significantly reduced compared to a standard algorithm. The sparsity of BE multi-domain systems is usually high, for

most of the models analyzed in this study it was above 50%.

The computed effective material constants from the SBS algorithm compared very well with results from both FE calculations and the simple rules of mixture equations. The strategy adopted for determining the displacement boundary condition for strain state 2 has been shown to be appropriate. The corresponding traction resultant in the 3 direction is less than 0.001% of that in the 2 direction for all cases analyzed, i.e. its relative value is approximately zero as it should be. Note that for estimating E_1 in the short-CNT-reinforced composite employing the rule of mixture, the length of the central part of the composite (containing polymer matrix and CNT) should be more appropriately taken as $l_c = l_{cyl}$, as the mechanism of load transmission to the fiber is basically by shear stress along the cylindrical surface of the CNT (see Fig. 11). In fact, values so estimated fit much better with those evaluated by the FE models [Chen and Liu (2004)] and the BE SBS technique.

Finally, a boundary element formulation is well suited to the study of composites. The determination of the effective elastic constants is dependent upon the surface stress solution, and as tractions are directly obtained from solving the boundary integral equations, this evaluation is straightforward. Moreover, for complex composites, surface meshes are simpler to generate than volume discretizations. Other important problems for composites, e.g., matrix-fiber interfacial bond, can be readily studied with the tools developed herein. The strategy is also adequate to model general anisotropic composites. Herein, special Green's functions for particular multilayered anisotropic solids [Yang and Pan (2002), Yuan, Yang, and Yang (2003), and Yang and Tewary (2006)] are not needed. With this in mind, it should be noted that the SBS algorithm can be promptly implemented on parallel-computing platforms [Ortiz, Shelton, Mantic, Paris, and Gray (2008)], and this should be a useful tool for analyzing large-scale/multi-scale composites. In Wang and Yao (2005), a BEM algorithm is also proposed to solve 3D RVEs of composites consisting of a number of

particles randomly dispersed inside a matrix material. There, a fast multipole method (FMM) is applied to accelerate the standard BEM, and future efficiency comparisons with the strategy presented in this paper are desirable.

References

Araújo, F. C.; Silva, K. I.; Telles, J. C. F. (2006): Generic domain decomposition and iterative solvers for 3D BEM problems. *Int. J. Numer. Methods Engrg.,* vol. 68, pp. 448-472.

Araújo, F. C.; Silva, K. I.; Telles, J. C. F. (2007): Application of a generic domain-decomposition strategy to solve shell-like problems through 3D BE models. *Commun. Numer. Meth. Engng.,* 23: 771–785.

Araújo, F. C.; Gray, L. J. (2008) Analysis of thin-walled structural elements via 3D standard BEM with generic substructuring. *Computational Mechanics* (in press).

Chen, X. L.; Liu, Y. J. (2004): Square representative volume elements for evaluating the effective material properties of carbon nanotube-based composites. *Computational Materials Science,* vol. 29, pp. 1-11.

Chen, X. L.; Liu, Y. J. (2005): An advanced 3D boundary element method for characterization of composite materials. *Eng. Anal. Boundary Elements,* vol. 29, pp. 513-523.

Chen, Y.; Dorgan Jr, B. L.; McIlroy, D. N.; Aston, D. E. (2006): On the importance of boundary conditions on nanomechanical bending behavior and elastic modulus determination of silver nanowires. *Journal of Applied Physics,* vol. 100, pp. 104301

Coutinho, A. L. G. A.; Martins, M. A. D.;

Sydenstricker, R. M.; Elias, R. N. (2006): Performance comparison of data-reordering algorithms for sparse matrix–vector multiplication in edge-based unstructured grid computations. *Int. J. Numer. Methods Engrg.,* vol. 66, pp. 431-460.

Elias, R. N.; Martins, M. A. D.; Coutinho, A. L. G. A. (2006): Parallel edge-based solution of viscoplastic flows with the SUPG/PSPG formulation. *Comput. Mech.,* vol. 38, pp. 365–381.

Fried, I. (1994): A gradient computational procedure for the solution of large problems arising from the finite element discretization method. *Int J Numer Methods Engrg.,* vol. 2, pp. 477-494.

Ghoniem, N. M.; Cho, K. (2002): The Emerging Role of Multiscale Modeling in Nano- and Micro-mechanics of Materials, *CMES: Computer Modeling in Engineering and Sciences*, vol. 3, pp. 147-174.

He, X. Q.; Kitipornchai, S.; Liew, K. M. (2005): Buckling analysis of multi-walled carbon nanotubes: a continuum model accounting for van der Waals interaction. *J. Mech. Phys. Solids*, vol. 53, pp. 303-326.

Hughes, T. J. R.; Levit, I.; Winget, L. (1983): An element-by-element solution algorithm for problems of structural and solid mechanics. *Comput. Methods Appl. Mech. Engrg.,* vol. 36 (2), pp. 241-254.

Hughes, T. J. R.; Ferencz, R. M.; Hallquist, J. O. (1987): Large-scale vectorized calculations in solid mechanics on a CRAY X-MP/48 utilizing EBE preconditioned conjugate gradients. *Comput. Methods Appl. Mech. Engrg.,* vol. 61, pp. 215-248.

Hyer, M. W. (1998): *Stress Analysis of Fiber-Reinforced Composite Materials*, 1st ed., McGraw-Hill, Boston.

Iijima, S. (1991): Helical microtubes of graphitics carbon. *Nature*, vol 354, pp. 56–8.

Kitipornchai, S.; He, X. Q.; Liew, K. M. (2005): Buckling analysis of triple-walled carbon nanotubes embedded in an elastic matrix. *J. Appl. Phys.* vol. 97, pp. 114318.

Lau, K.-T.; Chiparab, M.; Linga, H.-Y.; Hui, D. (2004): On the effective elastic moduli of

carbon nanotubes for nanocomposite structures. *Composites: Part B*, vol. 35, pp. 95–101.

Liu, Y. (1998): Analysis of shell-like structures by the boundary element method based on 3-D elasticity: formulation and verification. *Int. J. Numer. Methods Engrg.*, vol. 41, pp. 541-558.

Mansur, W. J.; Araújo, F. C.; Malaghini, J. E. B. (1992): Solution of BEM systems of equations via iterative techniques. *Int. J. Numer. Methods Engrg.*, vol. 33, pp. 1823-1841.

Namilae, S. ; Chandra, U.; Srinivasan, A.; Chandra, N. (2007): Effect of interface modification on the mechanical behavior of carbon nanotube reinforced composites using parallel molecular dynamics simulations. *CMES: Computer Modeling in Engineering and Sciences,* vol. 22(3), pp. 189-202.

Ortiz, J; Shelton, W. A.; Mantic, V. Paris, F.; Gray, L. J. (2008): A parallel domain decomposition BEM algorithm for three-dimensional exponentially graded elasticity. *Journal of Applied Mechanics* (in press)

Pantano, A.; Parks D. M.; Boyce, M. C. (2004): Mechanics of deformation of single and multiwall carbon nanotubes. J. Mech. Phys. Solids, vol 52, pp. 789-821.

Qian, D.; Dickey, E. C.; Andrews, R.; Rantell, T. (2000): Load transfer and deformation mechanisms in carbon nanotube-polystyrene composites. *Applied Physics Letter*, vol. 76, pp. 2868-2870.

Saad, Y. (2003): *Iterative Methods for Sparse Linear Systems*. Society for Industrial and Applied Mathematics (SIAM), Philadelphia.

Sleijpen, G. L. G., Fokkema D. R. (1993): BICGSTAB(L) for linear equations involving unsymmetric matrices with complex spectrum. *Electronic Trans. Num. Methods Anal.*, vol 1, pp. 11-32.

Srivastava1, D.; Atluri, S. N. (2002): Computational nanotechnology: a current perspective. *CMES: Computer Modeling in Engineering and Sciences,* vol. 3, pp. 531-538.

Telles, J. C. F. (1987): A self-adaptive co-ordinate transformation for efficient numerical evaluation of general boundary element integrals. *Int. J. Numer. Methods Engrg.,* vol 24, pp. 959-973.

van der Vorst, H. A. (2003): *Iterative Krylov Methods for Large Linear Systems*. Cambridge University Press.

Wang, C. M.; Ma, Y. Q.; Zhang, Y. Y.; Ang, K. K. (2006): Buckling of double-walled carbon nanotubes modeled by solid shell elements. *Journal of Applied Physics*, vol. 99, pp. 114317.

Wang, H.; Yao, Z. (2005): A New Fast Multipole Boundary Element Method for Large Scale Analysis of Mechanical Properties in 3D Particle-Reinforced Composites. *CMES: Computer Modeling in Engineering and Sciences,* vol.7(1), pp.85-95.

Yakobson, B. I.; Brabec, C. J.; Bernholc, J. (1996): Nanomechanics of carbon tubes: instabilities beyond linear response. *Physical Review Letters*, vol. 76, pp.2511-2514.

Yang, B.; Pan, E. (2002): Efficient evaluation of three-dimensional Green's functions in anisotropic elastostatic multilayered composites. *Engineering Analysis with Boundary Elements* vol. 26, pp. 355-366.

Yuan, F. G.; Yang, S.; Yang, B. (2003): Three-dimensional Green's functions for composite laminates. *Int. J. Solids and Structures*, vol. 40, pp. 331–342.

Yang, B.; Tewary, V.K. (2006): Efficient Green's function modeling of line and surface defects in multilayered anisotropic elastic and piezoelectric materials. *CMES: Computer Modeling in Engineering and Sciences,* vol. 15, pp. 165-177.

Zhang, S.-L. (2002): A class of product-type Krylov-subspace methods for solving nonsymmetric linear systems. *J. Comp. and Appl. Math.,* vol. 149, pp. 297–305.